

Kolmogorov-Crespi Potential For Multilayer Transition Metal Dichalcogenides: Capturing Structural Transformations In Moiré Superlattices.

Mit H. Naik, Indrajit Maity, Prabal K. Maiti, and Manish Jain*

*Center for Condensed Matter Theory, Department of Physics, Indian Institute of Science,
Bangalore 560012, India*

E-mail: mjain@iisc.ac.in

Abstract

We develop parameters for the interlayer Kolmogorov-Crespi (KC) potential to study structural features of four transition metal dichalcogenides (TMDs): MoS₂, WS₂, MoSe₂ and WSe₂. We also propose a mixing rule to extend the parameters to their heterostructures. Moiré superlattices of twisted bilayer TMDs have been recently shown to host shear solitons, topological point defects and ultraflatbands close to the valence band edge. Performing structural relaxations at the DFT level is a major bottleneck in the study of these systems. We show that the parametrized KC potential can be used to obtain atomic relaxations in good agreement with DFT relaxations. Furthermore, the moiré superlattices relaxed using DFT and the proposed forcefield yield very similar electronic band structures.

Introduction

The growing family of layered materials and the 'Lego set'¹ of possible heterostructures is an attractive field of research.^{2,3} Layered materials are composed of two-dimensional (2D) atomic layers weakly held together by van der Waals (vdW) forces. The widely used approach to theoretically simulate 2D materials and their heterostructures is through vdW corrected density functional theory⁴⁻⁷ (DFT). This quantum mechanics based approach is accurate but computationally intractable for applications that require large scale simulations of 2D materials with more than 10,000 atoms. One such application is the study of moiré patterns in 2D materials.

On introducing a small-angle twist between the two layers of a bilayer system leads to the formation of a large scale moiré superlattice (MSL).⁸⁻¹⁰ MSLs have interesting properties at the electronic as well as the structural level. The moiré pattern is composed of various local high-symmetry stackings.⁸⁻¹⁰ Structural reconstructions lead to the formation of shear strain solitons at stacking boundaries and topological point defects in twisted bilayer graphene (tBLG).^{8,11-14} Unconventional superconductivity was recently observed in tBLG

at a 'magic'¹⁵ twist angle due to the formation of ultraflatbands close to the Fermi level.¹⁶⁻¹⁹ Recent DFT calculations show that small-angle twisted bilayer TMDs can also host ultraflatbands, shear solitons and topological point defects.⁹ However, angles smaller than 3.5° could not be explored in this study⁹ due to higher computational cost. Obtaining the relaxed coordinates of the atoms in the MSL is a major bottle-neck in these calculations.

Classical force-field based methods have been used to replace expensive DFT calculations to study the structural properties of 2D materials.^{8,14,20-22} An important ingredient to classical force-field based methods is the proper modelling of the vdW interaction between layers.²³⁻²⁵ The Lennard-Jones (LJ) model has been widely used to account for the interlayer vdW interactions. Sliding one layer of a 2D material with respect to the other leads to different stacking configuration of the atoms, which have different binding energies. This stacking dependence of the binding energy is not captured by the LJ model. Tribology^{26,27} and the study of moiré patterns in 2D materials are particularly sensitive to the stacking dependence.^{28,29}

To overcome this drawback, the Kolmogorov-Crespi^{29,30} (KC) potential has been developed for bilayer graphene. This potential includes an additional stacking dependent term coupled with the short-range interaction. It has been successfully applied to graphene^{8,31,32} and BN³³ to explore solitons in moiré patterns,^{8,14} dislocations, shear modes, self-retraction³⁴⁻³⁶ and lubricity of graphene flakes^{27,37-39} and carbon nanotubes,^{22,27,29,40,41} etc. However, it has been restricted to these materials and not been extended to the vast family of transition metal dichalcogenides, and their heterostructures.^{42,43} We note that other methods like the continuum approach^{44,45} and a Gaussian-LJ⁴⁶ method have been developed to treat shear in bilayer MoS₂.

In this work, we parametrize the KC potential for multilayers of four transition metal dichalcogenides: MoS₂, MoSe₂, WS₂ and WSe₂. The Stillinger-Weber (SW)^{47,48} force field is used to model the constituent single layers and the KC potential determines the interlayer interactions. The KC parametrization is performed to fit the binding energy of the various

bilayer stackings computed using DFT. We also propose a mixing rule for these parameters to simulate heterostructures using these materials. The layer breathing mode and shear mode frequencies computed using these potentials are in good agreement with experiments. We use the SW and fitted KC parameters to perform the structural relaxation of the 3.5° and 56.5° twisted bilayer MoS₂. We find that the atomic relaxations using these forcefield calculations are in good agreement with relaxations performed using DFT. Furthermore, the electronic band structure computed using the forcefield relaxed structure is in good agreement with that computed using the DFT relaxed structure. Indicating that this method *can replace* the computationally expensive DFT relaxation steps while studying the electronic properties of moiré superlattices.

Computational Details

The vdW corrected DFT calculations are carried out using the plane-wave pseudopotential package Quantum Espresso.⁴⁹ We use ultrasoft⁵⁰ pseudopotentials and the local density approximation⁵¹ (LDA) for the exchange-correlation functional. The van der Waals interactions are computed using the van der Waals density functional^{52,53} along with Cooper⁵⁴ exchange (vdW-DF-C09).⁵⁵ We use a plane-wave energy cut-off of 50 Ry for the wavefunctions and a cut-off of 500 Ry for the charge density. The Brillouin zone is sampled with a $12 \times 12 \times 1$ k-point mesh. The DFT calculations are performed with the optimized geometry of the cell for each TMD. The forcefield calculations are performed using the LAMMPS^{56,57} package. The SW⁴⁸ potential is used for intralayer interactions and KC potential for interlayer interactions. The minimizations are performed using conjugate gradient method (force tolerance of 10^{-6} eV/) as implemented in LAMMPS with the DFT lattice constant. Parametrization of the KC potential to fit the DFT binding energy is performed with help of the Dakota^{58,59} package. Commensurate moiré superlattices of twisted bilayer MoS₂ are constructed using the Twister code.⁶⁰ KC potential file and LAMMPS input files for the

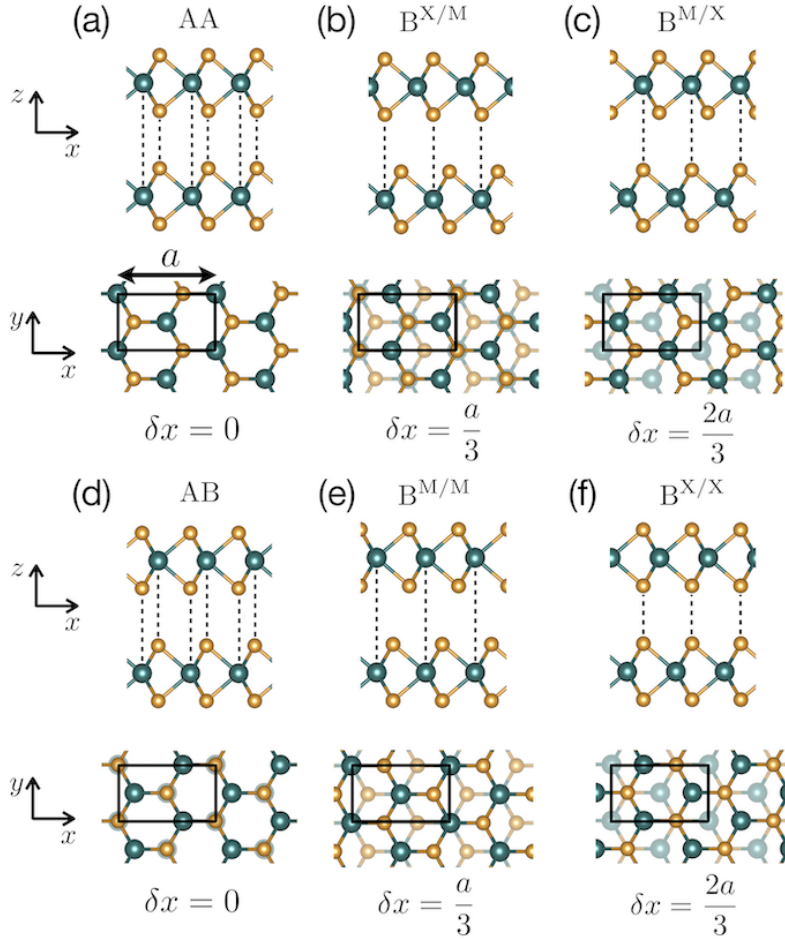


Figure 1: High-symmetry stackings of a bilayer TMD obtained by sliding the top layer with respect to the bottom layer. The orthogonal unit cell is marked. Starting with the AA stacking ($\delta x = \delta y = 0$) (a), sliding by $\delta x = a/3$ leads to the $B^{X/M}$ (b) stacking and sliding by $\delta x = 2a/3$ yields the $B^{M/X}$ (c) stacking. Similarly, starting with the AB (d) stacking yields $B^{M/M}$ (e) and $B^{X/X}$ (f) stackings.

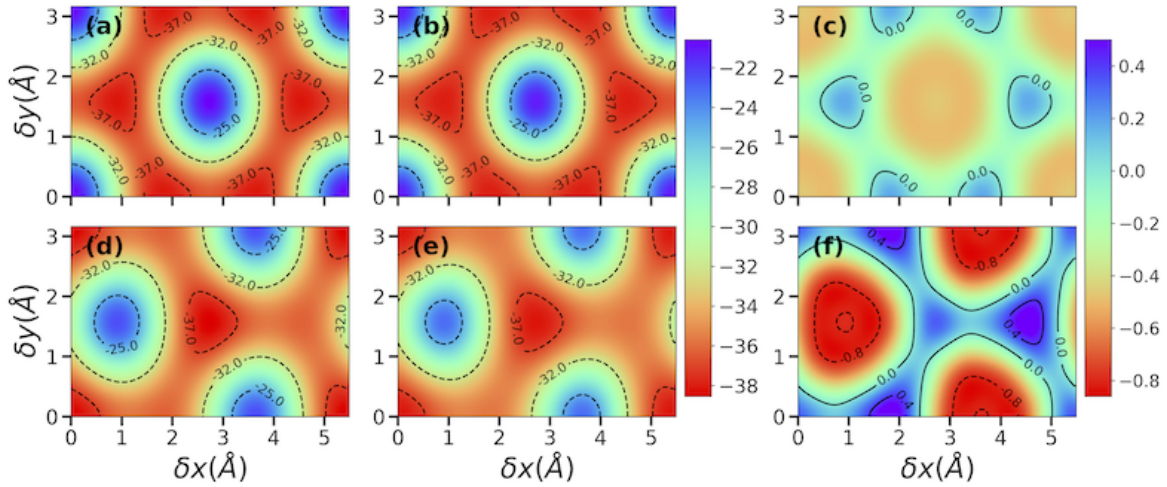


Figure 2: Binding energy (BE) (in meV/atom) as a function of sliding the top layer of bilayer MoS₂ with respect to the bottom layer along the x and y directions of the orthogonal unit cell. The interlayer spacing is fixed at 6.35 Å. The BE is computed as $(E_{\text{BL}} - 2E_{\text{SL}})/N$, where E_{BL} is the total energy of MoS₂ bilayer, E_{SL} is the energy of a monolayer and N is the number of atoms in the bilayer system. (a) and (d) BE landscape obtained using van der Waals corrected DFT. (b) and (e) BE landscape using Stillinger-Weber (SW) forcefield for intralayer interactions and KC for interlayer interactions. (c) and (f) Difference in the BE landscape computed using SW+KC and DFT. $(\delta x, \delta y) = (0, 0)$ is the AA (AB) stacking for (a), (b) and (c) ((d), (e) and (f)).

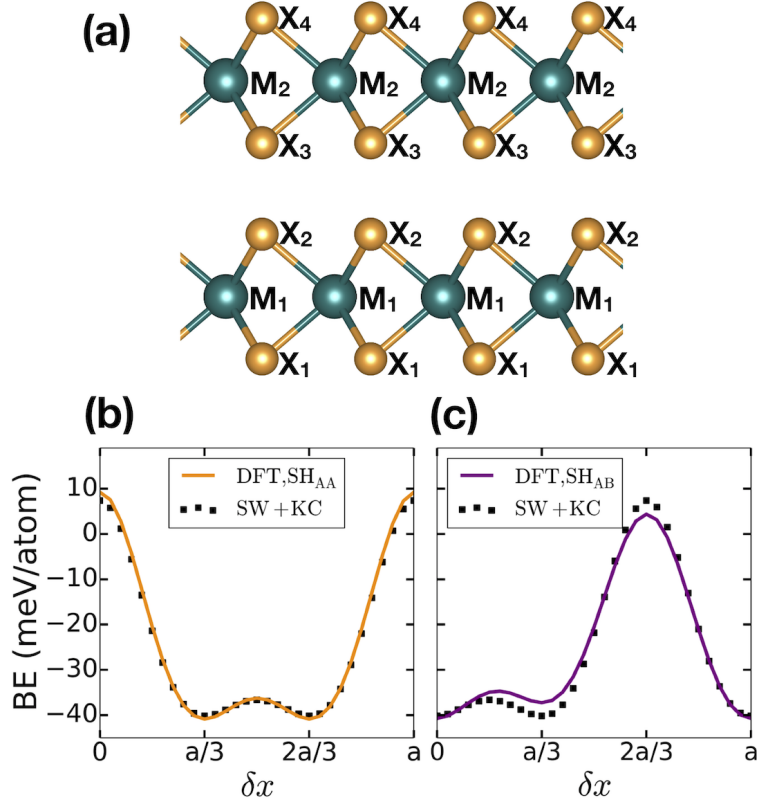


Figure 3: (a) Bilayer of a TMD with labels for each layer and type of atom. (b) BE computed using DFT and SW+KC^{S-S} of bilayer MoS₂ as a function of shear starting with the AA stacking, SH_{AA}. (c) BE computed using DFT and SW+KC^{S-S} of bilayer MoS₂ as a function of shear starting with the AB stacking, SH_{AB}. In (b) and (c) the KC interaction is considered only between the S₂ and S₃ atoms of bilayer MoS₂. The interlayer spacing is fixed at 6 Å.

bilayer TMDs are available with the Twister package.⁶⁰

Kolmogorov-Crespi potential

Fig. 1 shows the various possible high-symmetry stackings of a bilayer TMD system obtained by sliding one layer with respect to the other.⁹ The AA and AB stackings are obtained when atoms in the top layer are exactly above atoms in the bottom layer. In the case of AA stacking (Fig. 1 (a)), similar atoms are on top of one another (M on M and X on X), while in AB stacking (Fig. 1 (d)) dissimilar atoms are on top of one another (M on X and X on M). The other stackings are Bernal type (Fig. 1 (b), (c), (e) and (f)), ie. one atom in the top layer is in the hexagonal cavity of the bottom layer. In our notation, B^{M/X} implies a Bernal (B) stacking and that atom M in the top layer is directly above atom X in the bottom layer (Fig. 1 (c)). On starting with the AA stacking, we obtain B^{X/M} and B^{M/X} on sliding one layer with respect to the other in the x direction as shown in Fig. 1. We denote this shear by SH_{AA}. Note that B^{X/M} and B^{M/X} are equivalent stackings. On sliding, starting with AB stacked layers, two non-equivalent high-symmetry stackings are obtained: B^{M/M} and B^{X/X} (Fig. 1). We denote this shear by SH_{AB}. There are thus five unique high-symmetry stackings possible with TMDs in the 2H-phase.

We aim to model the binding energy (BE) landscape of the bilayer system as a function of shear between the two layers using classical forcefields. The BE landscape computed using vdW corrected DFT for bilayer MoS₂ with fixed interlayer spacing of 6.35 Å is shown in Fig. 2 (a) and (d). The Kolmogorov-Crespi is a reliable interlayer potential since it contains an explicit registry dependent term. The form of the potential is given by:

$$V_{ij} = e^{-\lambda(r_{ij}-z_0)}V_\rho - A \left(\frac{r_{ij}}{z_0} \right)^{-6} \quad (1)$$

The potential, V_{ij} , is defined between atom i in one layer and atom j in the adjacent layer. The potential is set to zero after a cut-off radius, r_{cut} . The KC potential includes a

stacking dependent term, V_ρ , multiplying the short-range repulsive interaction.

$$V_\rho = [C + f(\rho_{ij}) + f(\rho_{ji})], \quad (2)$$

where, $\rho_{ij}^2 = r_{ij}^2 - (\mathbf{n}_i \cdot \mathbf{r}_{ij})^2$, $\rho_{ji}^2 = r_{ij}^2 - (\mathbf{n}_j \cdot \mathbf{r}_{ij})^2$ and

$$f(\rho) = e^{(-\rho/\delta)^2} \sum_{n=0}^2 C_{2n} (\rho/\delta)^{2n} \quad (3)$$

V_ρ determines the energy barrier to shear one layer with respect to the other in a bilayer system. The KC potential thus consists of 8 parameters for each type of interaction. A taper function^{21,23,24,61} is often used to ensure the interlayer potential goes to zero smoothly. Using a large $r_{cut} = 14 \text{ \AA}$ does not affect the results significantly in the absence of the taper function. See Supplementary Information (SI) for more details. \mathbf{n}_i and \mathbf{n}_j are surface normals at site i and j , respectively. To compute the surface normal at the position of an atom i , we find the neighbours of the same type in a radius r_n around atom i . This is illustrated in Fig. 4. r_n is chosen to accommodate the six nearest neighbours of the same type. Six normals are then constructed from consecutive pairs of neighbouring atoms and averaged to obtain \mathbf{n}_i . See SI for more details. We refer to interactions that take into account the normals as KC-n. A simplification to the present form of the potential can be introduced by setting $\mathbf{n}_i = \mathbf{n}_j = \hat{z}$. This approximation only works for multilayers whose bending leads to normals that do not deviate significantly from \hat{z} . For the case of twisted bilayers, we find this to be a good approximation since the normals are close to \hat{z} . We will refer to this approximation as KC-z. This is discussed further in subsequent sections.

Steric effects govern the relative energy of the stackings. The stackings with chalcogen atoms in the top layer directly above chalcogen atoms in the bottom layer, ie. AA and B^{X/X}, are unfavourable and highest in energy.^{9,62} The other three stackings are relatively lower in energy. It would thus seem reasonable to consider the KC interactions between the X₂ and X₃ (Fig. 3 (a)) atoms alone. On fitting the KC parameters of this interaction, KC^{X-X}, to

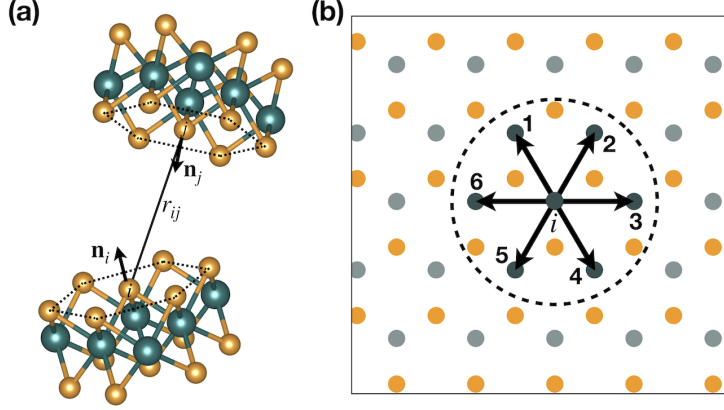


Figure 4: (a) Visual representation of the terms in the KC potential. The six nearest neighbours of the same type as i or j used to construct the normal are connected using dotted lines. (b) Computation of local normal for each atom, i , depending on its nearest-neighbor atoms of same type. For example, Mo atoms in MoS₂ forms a triangular lattice with six nearest-neighbour Mo atoms, chosen using a predefined cut-off radius r_n . Six normals are computed using consecutive pairs of the neighbour atoms: $\frac{\mathbf{r}_{1i} \times \mathbf{r}_{2i}}{|\mathbf{r}_{1i} \times \mathbf{r}_{2i}|}$, $\frac{\mathbf{r}_{2i} \times \mathbf{r}_{3i}}{|\mathbf{r}_{2i} \times \mathbf{r}_{3i}|}$, $\frac{\mathbf{r}_{3i} \times \mathbf{r}_{4i}}{|\mathbf{r}_{3i} \times \mathbf{r}_{4i}|}$, $\frac{\mathbf{r}_{4i} \times \mathbf{r}_{5i}}{|\mathbf{r}_{4i} \times \mathbf{r}_{5i}|}$, $\frac{\mathbf{r}_{5i} \times \mathbf{r}_{6i}}{|\mathbf{r}_{5i} \times \mathbf{r}_{6i}|}$ and $\frac{\mathbf{r}_{6i} \times \mathbf{r}_{1i}}{|\mathbf{r}_{6i} \times \mathbf{r}_{1i}|}$. The local normal is finally computed after averaging over the six normals for i -th atom.

DFT BE leads to a good representation of shear starting with the AA stacking (SH_{AA}), as shown in Fig. 3 (b). But fails to completely represent the BE of shear starting with the AB stacking (Fig. 3 (c)). In particular, the difference in BE between AB and B^{M/M} stackings is not captured. This is expected, because in the presence of only X₂-X₃ interactions, AB stacking is indistinguishable from the B^{M/M} stacking.

To differentiate the BE of the AB and B^{M/M} stackings in SH_{AB} we further introduce the M₁-X₃, M₂-X₂ and M₁-M₂ interlayer interactions (see Fig. 3 (a)). We introduce these additional interactions and refit all the KC parameters. In the supplementary information we propose two other approaches to obtain the BE landscape with reasonable accuracy. The first includes only X₂-X₃ and M₁-M₂ interactions, KC_{M-M}^{X-X} , and the second approach includes only X₂-X₃, M₁-X₃ and M₂-X₂ interactions, KC_{M-X}^{X-X} . We have also fit KC_{M-M}^{X-X} parameters including the taper function discussed above. KC_{M-M}^{X-X} and KC_{M-X}^{X-X} parameters are provided and further discussed in the supplementary information. For the rest of the article, we will show the performance of the parametrized KC potential when all interlayer interactions,

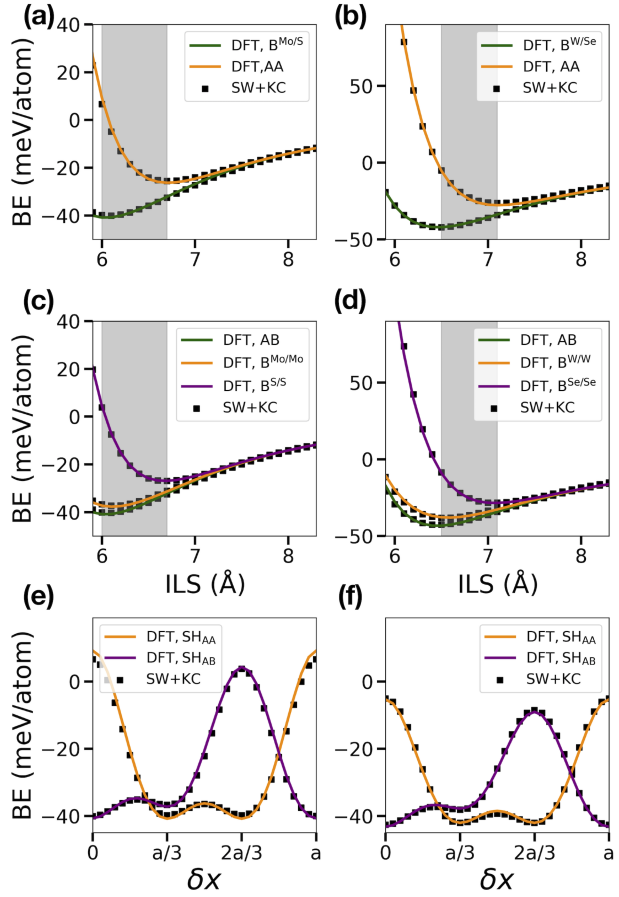


Figure 5: (a) and (c) ((b) and (d)) BE computed within DFT and using SW+KC as a function of interlayer spacing for the high-symmetry stackings in bilayer MoS₂ (WSe₂). The shaded region marks the range of interlayer spacings in the bilayer system. (e) ((f)) BE computed within DFT and using SW+KC as a function of shear, SH_{AA} and SH_{AB}, in bilayer MoS₂ (WSe₂). The ILS in (e) and (f) is fixed to 6.0 and 6.5 Å.

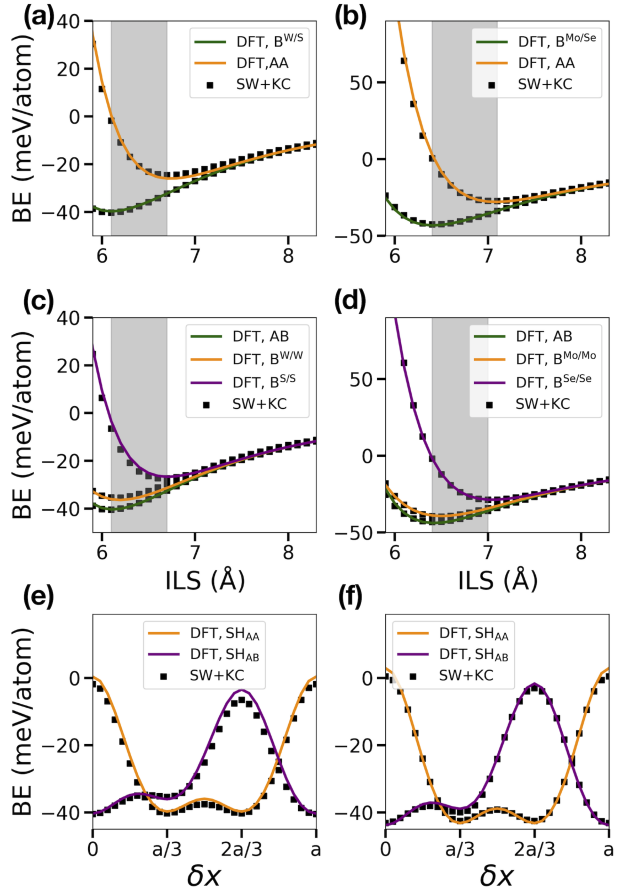


Figure 6: (a) and (c) ((b) and (d)) BE computed within DFT and using SW+KC as a function of interlayer spacing for the high-symmetry stackings in bilayer WS₂ (MoSe₂). The shaded region marks the range of interlayer spacings in the bilayer system. (e) ((f)) BE computed within DFT and using SW+KC as a function of shear, SH_{AA} and SH_{AB}, in bilayer WS₂ (MoSe₂). The ILS in (e) and (f) is fixed to 6.0 and 6.4 Å.

X_2 - X_3 , M_1 - X_3 , M_2 - X_2 and M_1 - M_2 , are included. These parameters are provided in Table 1. The BE landscape for MoS₂ with SW+KC is shown in Fig. 2 (b) and (e). Fig. 2 (c) and (f) show the deviation of the landscape computed using SW+KC from DFT.

Table 1: Parameters for interlayer Kolmogorov-Crespi interactions.

	z_0 (Å)	C_0 (meV)	C_2 (meV)	C_4 (meV)	C (meV)	δ (Å)	λ (Å ⁻¹)	A (meV)
S ₂ -S ₃	3.857	7.074	2.624	0.024	24.859	0.982	2.762	55.637
Se ₂ -Se ₃	3.992	7.886	6.355	-0.011	26.762	0.935	2.753	60.829
Mo ₁ -S ₃ , Mo ₂ -S ₂	4.049	-2.718	-2.719	-0.325	16.459	0.616	2.564	14.239
Mo ₁ -Se ₃ , Mo ₂ -Se ₂	5.080	-1.120	-0.761	-0.117	4.624	0.777	1.996	6.209
W ₁ -S ₃ , W ₂ -S ₂	4.331	-1.344	-1.370	-0.162	8.372	0.587	2.082	7.078
W ₁ -Se ₃ , W ₂ -Se ₂	5.079	-1.109	-0.762	-0.120	4.627	0.783	1.999	5.112
Mo ₁ -Mo ₂	9.236	1.471	1.126	0.131	1.928	1.183	0.924	3.439
W ₁ -W ₂	10.545	0.254	0.139	-0.028	0.506	1.010	0.944	1.356

Table 2: Comparison of the shear (SM) and layer breathing modes (LBM) of bilayer TMDs computed using SW+KC with experimental measurements.

	LBM (cm ⁻¹)	
	SW+KC	Expt.
BLMoS ₂	38.6	40, ⁶³ 41.6 ⁶⁴
BLWS ₂	30.5	33.8 ⁶⁴
BLMoSe ₂	31.0	34.3, ⁶⁴ 29 ⁶⁵
BLWSe ₂	27.2	29.1, ⁶⁴ 27 ⁶⁵
	SM (cm ⁻¹)	
	SW+KC _{M-M} ^{X-X}	Expt.
BLMoS ₂	20.9	22, ⁶³ 24.2 ⁶⁴
BLWS ₂	18.0	19.6 ⁶⁴
BLMoSe ₂	18.3	21, ⁶⁴ 18 ⁶⁵
BLWSe ₂	15.7	17.7, ⁶⁴ 17 ⁶⁵

The KC potential parameters are obtained by fitting the BE as a function of interlayer spacing (out-of-plane separation between M atoms of top and bottom layer) for the high-symmetry stackings and as a function of shear between the two layers, SH_{AA} and SH_{AB}. The fitting to the shear is performed at the average interlayer spacing of the high-symmetry stackings. Fitting shear at the average interlayer spacing is sufficient to reproduce the shear at the minimum and maximum interlayer spacings as well. Fig. 5 (a), (c) and (e) compare

the BE computed using SW+KC with the corresponding DFT BE for bilayer MoS₂. Fig. 5 (b), (d) and (f) compares SW+KC BE with DFT for bilayer WSe₂. Fig. 6 similarly shows the performance of the KC parameters for bilayer WS₂ and MoSe₂. Furthermore, the shear and layer breathing modes⁶⁶ of the bilayer TMDs computed using SW+KC are in good agreement with experimental measurements (Table 2). See supplementary information for the performance of the other set of parameters: KC_{M-M}^{X-X} and KC_{M-X}^{X-X} .

Heterostructures: mixing rule

Mechanical exfoliation⁶⁷ and chemical vapour deposition⁶⁸⁻⁷⁰ techniques can be used to construct vertical stacks⁷¹ of different TMDs. These heterostructures generally form a Type II heterojunction,⁶⁷ which makes them suitable for applications in nano- and opto-electronics.⁷¹ The KC parameters developed above for the bilayer TMDs can be extended to heterostructures by the use of a simple mixing rule. The cross-interaction parameters for S-Se are obtained by taking the arithmetic mean (AM) of S-S and Se-Se parameters. Similarly the Mo-W interaction are computed as an AM of Mo-Mo and W-W parameters. We tried other mixing rules like the geometric mixing rule and find that the AM works best to reproduce the DFT BE.

We apply the mixing rule to simulate the MoS₂/MoSe₂ and MoS₂/WS₂ heterostructure. MoS₂ and MoSe₂ are not lattice matched. For the purpose of comparison, we strain the layers to their average lattice constants in the DFT and forcefield calculations. We compute the BE as a function of interlayer spacing and shear as shown in Fig. 7 for MoS₂/MoSe₂ and MoS₂/WS₂ heterostructure. AA stacking in the context of heterostructures implies transition metal (chalcogen) atom in the top layer is above a transition metal (chalcogen) atom in the bottom layer. AB stacking implies transition metal (chalcogen) atom in the top layer is above a chalcogen (transition metal) atom in the bottom layer. The BE computed using SW+KC is in good agreement with DFT (Fig. 7).

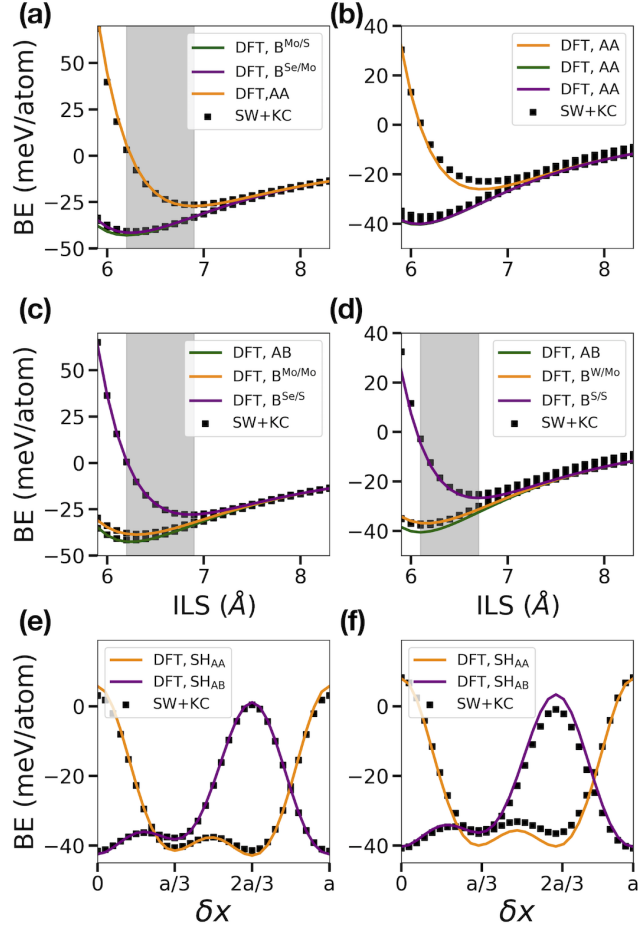


Figure 7: (a) and (c) ((b) and (d)) BE computed within DFT and using SW+KC as a function of interlayer spacing (ILS) for different stackings in the heterostructure MoS₂/MoSe₂ (MoS₂/WS₂). The shaded region marks the range of possible interlayer spacings in the heterostructure. (e) ((f)) BE computed within DFT and using SW+KC as a function of shear, SH_{AA} and SH_{AB}, for MoS₂/MoSe₂ (MoS₂/WS₂) The ILS here is fixed to that of the minimum ILS among the high-symmetry stackings.

Moiré superlattices

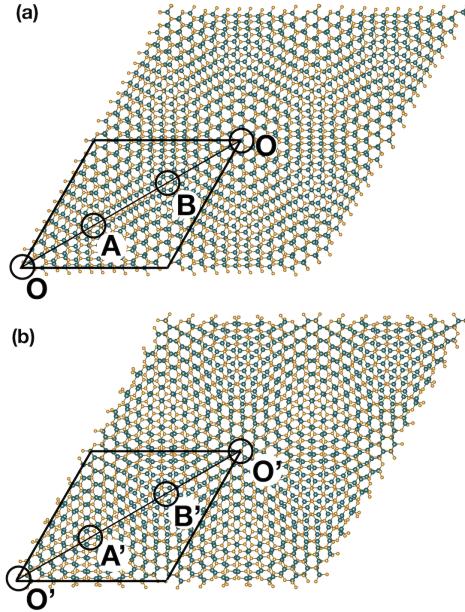


Figure 8: (a) and (b) Moiré superlattice (MSL) obtained on twisting bilayer MoS₂ by 5.1° and 54.9°, respectively. Marked with circles are the high-symmetry stackings in the MSL.

Twisted bilayer TMDs form distinct moiré patterns for twist angles close to 0° and 60°.^{9,72,73} Fig. 8 shows the MSL for 5.1° (M^{5.1}) and 54.9° (M^{54.9}) twists. The MSL is composed of the various high-symmetry stackings (Fig. 1).⁹ The regions O, A and B are AA, B^{X/M} and B^{M/X} respectively. The regions O', A' and B' are AB, B^{M/M} and B^{X/X} respectively. Relaxing these moiré patterns in DFT starting from the rigidly twisted structure leads to significant in-plane and out-of-plane displacements of the atoms.⁹ Because of large bending rigidity,⁶⁶ the out-of-plane displacements smoothly vary across the MSL surface. The ILS is largest for the AA and B^{S/S} stacking regions as shown in Fig. 9 (e) for the case of 3.5° twisted bilayer MoS₂. We also use the SW+KC to perform the relaxations of the same MSL, starting with the rigidly twisted structure. The ILS distribution obtained using the forcefield approach (Fig. 9 (f)) is in good agreement with the DFT results. We have performed these relaxation using KC-n, ie. including normals in the interlayer interaction.

The undulations in each of the layers is smooth. The out-of-plane displacements of each

layer, while significant, vary over a large area. We thus find that the normals do not deviate significantly from \hat{z} for small or large twist-angles. The distribution of ϕ in KC-n relaxed structures is shown in Fig. 11 for a relatively large (7.3°) and small (1°) twist angle MSL. For angles greater than 7.3° and smaller than 52.7° , the out-of-plane displacements are small. ϕ takes a maximum value of 1.2° in Fig. 11, and $\cos(1.2^\circ) \approx 1$. Furthermore, we find the energy computed using KC-n and KC-z for these angles differ by less than 0.01 meV/atom. KC-z is thus sufficient to capture relaxations in moiré superlattices. We also compare the forces in the MSL computed using DFT, KC-n and KC-z for unrelaxed 7.3° twisted bilayer MoS_2 in Fig. 12. The out-of-plane forces are in excellent agreement between DFT and the proposed forcefields.

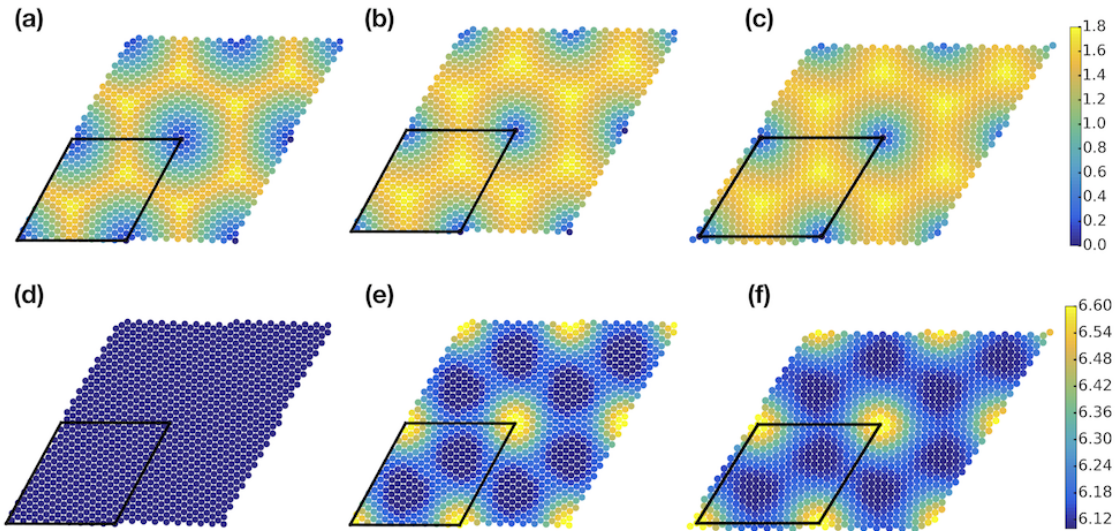


Figure 9: Distribution of interlayer spacings (ILS) and order-parameter (OP) in the MSL. (a) and (d) OP and ILS distribution in the rigidly-twisted bilayer MoS_2 . The twist angle here is 3.5° . Black lines mark the MSL. (b) and (e) ((c) and (f)) Distribution of OP and ILS in the MSL relaxed using DFT (SW+KC), respectively. The normals are taken into account in the interlayer KC interaction.

The in-plane displacements of the MoS_2 units in the moiré pattern lead to an increase in the area of low-energy stacking with respect to the rigidly twisted MSL.⁹ The stackings in the relaxed structure can be identified by means of an order-parameter (OP). The OP is defined⁹ as the shortest displacement vector that takes any given stacking in the moiré

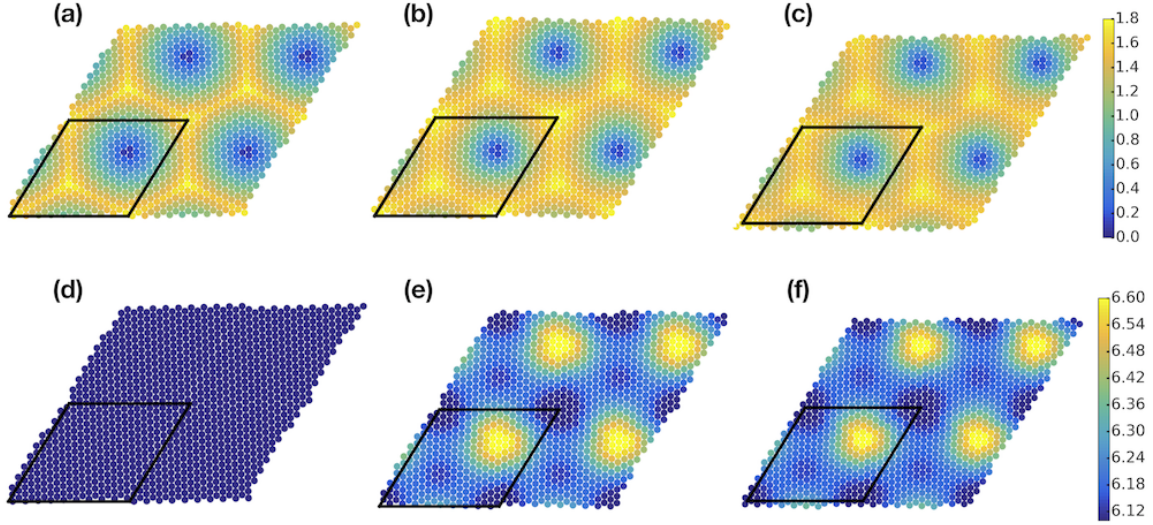


Figure 10: Distribution of interlayer spacings (ILS) and order-parameter (OP) in the MSL. (a) and (d) OP and ILS distribution in the rigidly-twisted bilayer MoS₂. The twist angle here is 56.5°. (b) and (e) ((c) and (f)) Distribution of OP and ILS in the MSL relaxed using DFT (SW+KC), respectively. The normals are taken into account in the interlayer interaction.

pattern to the highest energy stacking. We define \vec{u} for the moiré pattern formed by twist angles close to 0° and \vec{v} for those formed by twist angles close to 60°. Hence \vec{u} is the shortest displacement vector that takes any given stacking in M^{3.5} to AA stacking and \vec{v} is the shortest displacement vector that takes any given stacking in M^{56.5} to B^{S/S}.⁹ Fig. 9 (a) shows the OP distribution for the rigidly twisted MSL, M^{3.5}. The distribution of the OP in the DFT relaxed MSL (Fig. 9 (b)) is in good agreement with that in the SW+KC_{Mo-S}^{S-S} relaxed MSL (Fig. 9 (c)). This indicates that the registry of atoms are similar in the MSL relaxed within DFT and the forcefield. OP and ILS using the other set of parameters, KC_{Mo-Mo}^{S-S} and KC_{Mo-S}^{S-S}, are also in good agreement with DFT (see supporting information).

The electronic structure of MSLs in bilayers⁹ as well as heterostructures⁷⁴ has been shown to host flat bands close to the valence band edge. We demonstrate that the electronic structure calculations can replace the time-consuming relaxation steps in DFT with the forcefield relaxations. To this effect, we compute the band structure of 7.3°, 9.4°, 50.6°, 52.7° twisted MSL using the DFT relaxed structure and the structure from SW+KC relaxations.

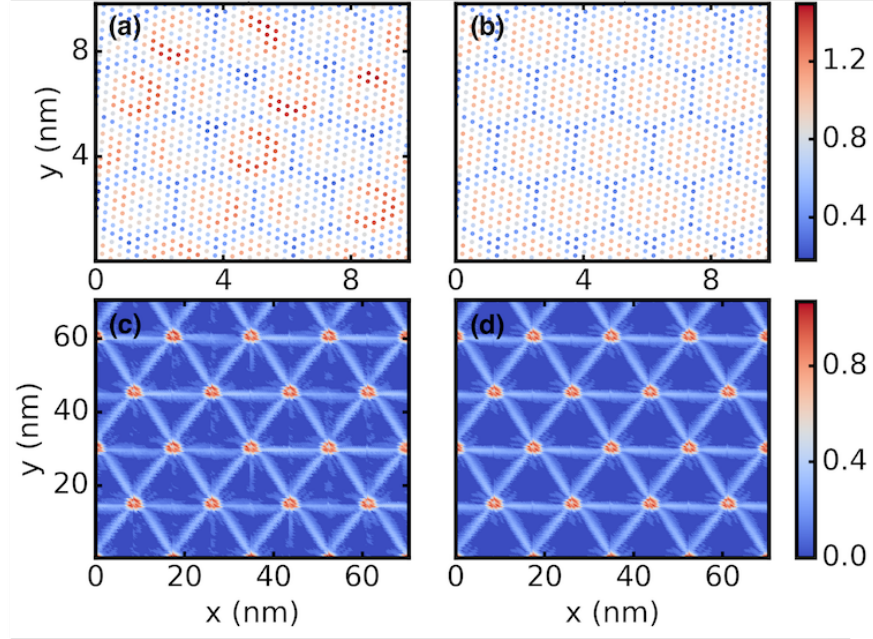


Figure 11: Distribution of the angular deviation, ϕ of the local unit-normal from the global \hat{z} direction (i.e. $n \cdot \hat{z} = \cos(\phi)$) for M_1 atoms in the MSL. (a) and (b) ϕ computed for 7.3° twisted bilayer MoS₂, relaxed using KC-n and KC-z, respectively. (c) and (d) ϕ computed for 1.0° twisted bilayer MoS₂, relaxed using KC-n and KC-z, respectively. The relaxations are performed using SW+KC. The colorbar shows the limits of the angular deviation distribution.

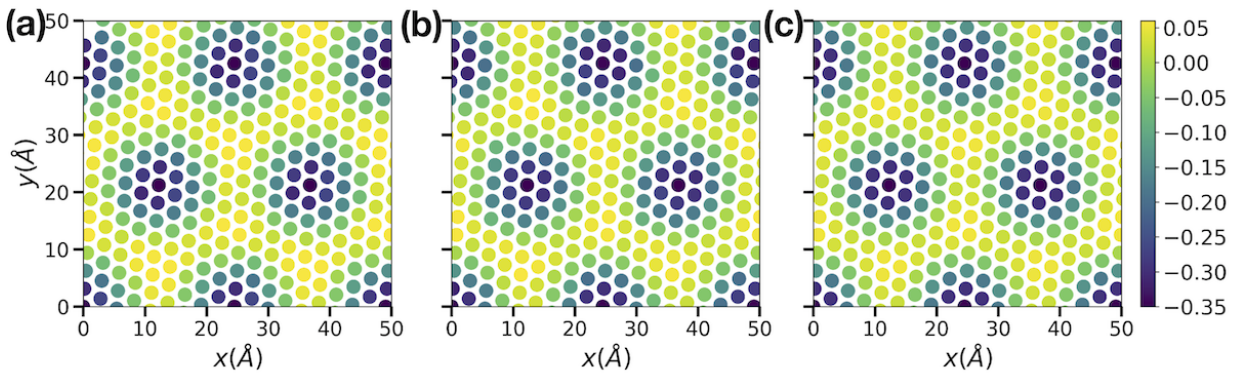


Figure 12: Distribution of the out-of-plane component of forces, f_z (in eV/Å), in 7.3° rigidly twisted bilayer MoS₂ (unrelaxed). f_z is shown for the S₂ atom type in the bottom layer. (a) Computed using vdW corrected DFT. (b) and (c) Computed using SW+KC-n and SW+KC-z, respectively.

We find that these band structures are in good agreement as shown in Fig. 13.

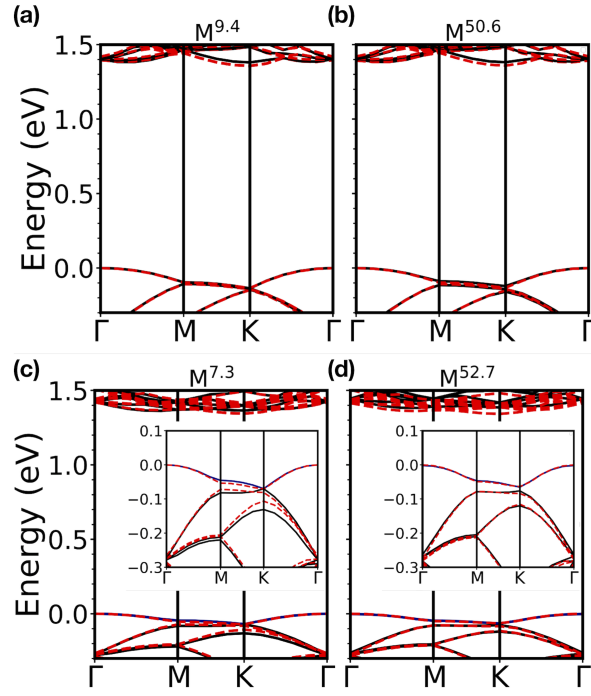


Figure 13: (a) and (b) Electronic band structure of 9.4° and 50.6° twisted bilayer MoS_2 , respectively. (c) and (d) Band structure of 7.3° and 52.7° twisted bilayer MoS_2 , respectively. Solid lines represent band structure computed using the DFT relaxed structure. Dashed lines represent the band structure computed using the forcefield (SW+KC) relaxed structure. The inset shows an enlarged plot of the valence bands in $M^{7.3}$ and $M^{52.7}$. The flat band is marked in blue.

In conclusion, we parametrize the KC potential for multilayer TMDs and propose a mixing rule to extend the parameter to TMD heterostructures. The parametrization is performed to fit the BE landscape computed using van der Waals corrected DFT. We show that the forcefield can be used to simulate structural transformations in MSLs of twisted bilayer MoS_2 . These structural reconstructions are in good agreement with those computed using DFT. Furthermore, the electronic band structure computed using the forcefield relaxed structure is in good agreement with band structure computed using the DFT relaxed structure. This indicates that the computationally expensive DFT relaxation steps can be replaced by the proposed forcefield method. Apart from predicting the structure of MSLs, several tribological properties can be studied using these KC potentials. The lubricity of the

various bilayers and bilayer heterostructures can be computed. Moreover, the dependence of lubricity on the twist angle between the bilayers can be explored. The effect of finite temperature on the tribological properties and on solitons in the MSLs can also be studied with molecular dynamics simulations using these potentials.

Acknowledgement

We thank the Supercomputer Education and Research Centre (SERC) at IISc for providing the computational facilities.

Supporting Information Available

The following files are available free of charge. Supporting Information. Verification of computation of normals with periodically modulated MoS₂ sheet; alternate parameter sets KC_{M-M}^{X-X} and KC_{M-X}^{X-X} ; performance of the alternate parameter sets; table containing number of atoms in the MSL and MSL dimension; ILS, OP and electronic band structure of the MSL using $SW+KC_{Mo-Mo}^{S-S}$ for twisted bilayer MoS₂; refitted parameters with the taper function for KC_{M-M}^{X-X} .

References

- (1) Geim, A. K.; Grigorieva, I. V. Van der Waals heterostructures. *Nature* **2013**, *499*, 419.
- (2) Novoselov, K. S.; Mishchenko, A.; Carvalho, A.; Castro Neto, A. H. 2D materials and van der Waals heterostructures. *Science* **2016**, *353*.
- (3) Sun, Z.; Martinez, A.; Wang, F. Optical modulators with 2D layered materials. *Nature Photonics* **2016**, *10*, 227.

- (4) Kohn, W.; Sham, L. J. Self-Consistent Equations Including Exchange and Correlation Effects. *Phys. Rev.* **1965**, *140*, A1133–A1138.
- (5) Qian, X.; Wang, Y.; Li, W.; Lu, J.; Li, J. Modelling of stacked 2D materials and devices. *2D Materials* **2015**, *2*, 032003.
- (6) Björkman, T.; Gulans, A.; Krasheninnikov, A. V.; Nieminen, R. M. Are we van der Waals ready? *Journal of Physics: Condensed Matter* **2012**, *24*, 424218.
- (7) Naik, M. H.; Jain, M. Substrate screening effects on the quasiparticle band gap and defect charge transition levels in MoS₂. *Phys. Rev. Materials* **2018**, *2*, 084002.
- (8) Gargiulo, F.; Yazyev, O. V. Structural and electronic transformation in low-angle twisted bilayer graphene. *2D Materials* **2018**, *5*, 015019.
- (9) Naik, M. H.; Jain, M. Ultraflatbands and Shear Solitons in Moiré Patterns of Twisted Bilayer Transition Metal Dichalcogenides. *Phys. Rev. Lett.* **2018**, *121*, 266401.
- (10) Kang, P.; Zhang, W.-T.; Michaud-Rioux, V.; Kong, X.-H.; Hu, C.; Yu, G.-H.; Guo, H. Moiré impurities in twisted bilayer black phosphorus: Effects on the carrier mobility. *Phys. Rev. B* **2017**, *96*, 195406.
- (11) Yankowitz, M.; Wang, J. I.-J.; Birdwell, A. G.; Chen, Y.-A.; Watanabe, K.; Taniguchi, T.; Jacquod, P.; San-Jose, P.; Jarillo-Herrero, P.; LeRoy, B. J. Electric field control of soliton motion and stacking in trilayer graphene. *Nature Materials* **2014**, *13*, 786.
- (12) San-Jose, P.; Gorbachev, R. V.; Geim, A. K.; Novoselov, K. S.; Guinea, F. Stacking Boundaries and Transport in Bilayer Graphene. *Nano Letters* **2014**, *14*, 2052–2057.
- (13) Alden, J. S.; Tsen, A. W.; Huang, P. Y.; Hovden, R.; Brown, L.; Park, J.; Muller, D. A.; McEuen, P. L. Strain solitons and topological defects in bilayer graphene. *Proceedings of the National Academy of Sciences* **2013**, *110*, 11256–11260.

- (14) van Wijk, M. M.; Schuring, A.; Katsnelson, M. I.; Fasolino, A. Relaxation of moiré patterns for slightly misaligned identical lattices: graphene on graphite. *2D Materials* **2015**, *2*, 034010.
- (15) Bistritzer, R.; MacDonald, A. H. Moiré bands in twisted double-layer graphene. *Proceedings of the National Academy of Sciences* **2011**, *108*, 12233–12237.
- (16) Cao, Y.; Fatemi, V.; Fang, S.; Watanabe, K.; Taniguchi, T.; Kaxiras, E.; Jarillo-Herrero, P. Unconventional superconductivity in magic-angle graphene superlattices. *Nature* **2018**, *556*, 43.
- (17) Cao, Y.; Fatemi, V.; Demir, A.; Fang, S.; Tomarken, S. L.; Luo, J. Y.; Sanchez-Yamagishi, J. D.; Watanabe, K.; Taniguchi, T.; Kaxiras, E. et al. Correlated insulator behaviour at half-filling in magic-angle graphene superlattices. *Nature* **2018**, *556*, 80.
- (18) Kennes, D. M.; Lischner, J.; Karrasch, C. Strong correlations and $d + id$ superconductivity in twisted bilayer graphene. *Phys. Rev. B* **2018**, *98*, 241407.
- (19) Wu, F.; MacDonald, A. H.; Martin, I. Theory of Phonon-Mediated Superconductivity in Twisted Bilayer Graphene. *Phys. Rev. Lett.* **2018**, *121*, 257001.
- (20) Zhu, S.; Johnson, H. T. Moiré-templated strain patterning in transition-metal dichalcogenides and application in twisted bilayer MoS₂. *Nanoscale* **2018**, *10*, 20689–20701.
- (21) Ouyang, W.; Mandelli, D.; Urbakh, M.; Hod, O. Nanoserpents: Graphene Nanoribbon Motion on Two-Dimensional Hexagonal Materials. *Nano Letters* **2018**, *18*, 6009–6016.
- (22) Guerra, R.; Leven, I.; Vanossi, A.; Hod, O.; Tosatti, E. Smallest Archimedean Screw: Facet Dynamics and Friction in Multiwalled Nanotubes. *Nano Letters* **2017**, *17*, 5321–5328.

- (23) Leven, I.; Azuri, I.; Kronik, L.; Hod, O. Inter-layer potential for hexagonal boron nitride. *The Journal of Chemical Physics* **2014**, *140*, 104106.
- (24) Leven, I.; Maaravi, T.; Azuri, I.; Kronik, L.; Hod, O. Interlayer Potential for Graphene/h-BN Heterostructures. *Journal of Chemical Theory and Computation* **2016**, *12*, 2896–2905.
- (25) Marom, N.; Bernstein, J.; Garel, J.; Tkatchenko, A.; Joselevich, E.; Kronik, L.; Hod, O. Stacking and Registry Effects in Layered Materials: The Case of Hexagonal Boron Nitride. *Phys. Rev. Lett.* **2010**, *105*, 046801.
- (26) Feng, X.; Kwon, S.; Park, J. Y.; Salmeron, M. Superlubric Sliding of Graphene Nanoflakes on Graphene. *ACS Nano* **2013**, *7*, 1718–1724.
- (27) Zhai, W.; Srikanth, N.; Kong, L. B.; Zhou, K. Carbon nanomaterials in tribology. *Carbon* **2017**, *119*, 150 – 171.
- (28) Leven, I.; Krepel, D.; Shemesh, O.; Hod, O. Robust Superlubricity in Graphene/h-BN Heterojunctions. *The Journal of Physical Chemistry Letters* **2013**, *4*, 115–120.
- (29) Kolmogorov, A. N.; Crespi, V. H. Registry-dependent interlayer potential for graphitic systems. *Phys. Rev. B* **2005**, *71*, 235415.
- (30) Kolmogorov, A. N.; Crespi, V. H. Smoothest Bearings: Interlayer Sliding in Multiwalled Carbon Nanotubes. *Phys. Rev. Lett.* **2000**, *85*, 4727–4730.
- (31) van Wijk, M. M.; Schuring, A.; Katsnelson, M. I.; Fasolino, A. Moiré Patterns as a Probe of Interplanar Interactions for Graphene on h-BN. *Phys. Rev. Lett.* **2014**, *113*, 135504.
- (32) Choi, Y. W.; Choi, H. J. Strong electron-phonon coupling, electron-hole asymmetry, and nonadiabaticity in magic-angle twisted bilayer graphene. *Phys. Rev. B* **2018**, *98*, 241412.

- (33) Maaravi, T.; Leven, I.; Azuri, I.; Kronik, L.; Hod, O. Interlayer Potential for Homogeneous Graphene and Hexagonal Boron Nitride Systems: Reparametrization for Many-Body Dispersion Effects. *The Journal of Physical Chemistry C* **2017**, *121*, 22826–22835.
- (34) Zheng, Q.; Jiang, B.; Liu, S.; Weng, Y.; Lu, L.; Xue, Q.; Zhu, J.; Jiang, Q.; Wang, S.; Peng, L. Self-Retracting Motion of Graphite Microflakes. *Phys. Rev. Lett.* **2008**, *100*, 067205.
- (35) Popov, A. M.; Lebedeva, I. V.; Knizhnik, A. A.; Lozovik, Y. E.; Potapkin, B. V. Molecular dynamics simulation of the self-retracting motion of a graphene flake. *Phys. Rev. B* **2011**, *84*, 245437.
- (36) Wang, D.; Chen, G.; Li, C.; Cheng, M.; Yang, W.; Wu, S.; Xie, G.; Zhang, J.; Zhao, J.; Lu, X. et al. Thermally Induced Graphene Rotation on Hexagonal Boron Nitride. *Phys. Rev. Lett.* **2016**, *116*, 126101.
- (37) Koren, E.; Duerig, U. Moiré scaling of the sliding force in twisted bilayer graphene. *Phys. Rev. B* **2016**, *94*, 045401.
- (38) Koren, E.; Duerig, U. Superlubricity in quasicrystalline twisted bilayer graphene. *Phys. Rev. B* **2016**, *93*, 201404.
- (39) van Wijk, M. M.; de Wijn, A. S.; Fasolino, A. Collective superlubricity of graphene flakes. *Journal of Physics: Condensed Matter* **2016**, *28*, 134007.
- (40) Xia, D.; Luo, Y.; Li, Q.; Xue, Q.; Zhang, X.; Liang, C.; Dong, M. Extracting the inner wall from nested double-walled carbon nanotube by platinum nanowire: molecular dynamics simulations. *RSC Adv.* **2017**, *7*, 39480–39489.
- (41) Oz, I.; Leven, I.; Itkin, Y.; Buchwalter, A.; Akulov, K.; Hod, O. Nanotube Motion on Layered Materials: A Registry Perspective. *The Journal of Physical Chemistry C* **2016**, *120*, 4466–4470.

- (42) Nicolini, P.; Polcar, T. A comparison of empirical potentials for sliding simulations of MoS₂. *Computational Materials Science* **2016**, *115*, 158 – 169.
- (43) Levita, G.; Molinari, E.; Polcar, T.; Righi, M. C. First-principles comparative study on the interlayer adhesion and shear strength of transition-metal dichalcogenides and graphene. *Phys. Rev. B* **2015**, *92*, 085434.
- (44) Carr, S.; Massatt, D.; Torrisi, S. B.; Cazeaux, P.; Luskin, M.; Kaxiras, E. Relaxation and domain formation in incommensurate two-dimensional heterostructures. *Phys. Rev. B* **2018**, *98*, 224102.
- (45) Cazeaux, P.; Luskin, M.; Massatt, D. Energy minimization of 2D incommensurate heterostructures. *arXiv preprint arXiv:1806.10395* **2018**,
- (46) Jiang, J.-W.; Park, H. S. A Gaussian treatment for the friction issue of Lennard-Jones potential in layered materials: Application to friction between graphene, MoS₂, and black phosphorus. *Journal of Applied Physics* **2015**, *117*, 124304.
- (47) Stillinger, F. H.; Weber, T. A. Computer simulation of local order in condensed phases of silicon. *Phys. Rev. B* **1985**, *31*, 5262–5271.
- (48) Jiang, J.-W.; Zhou, Y.-P. In *Handbook of Stillinger-Weber Potential Parameters for Two-Dimensional Atomic Crystals*; Jiang, J.-W., Zhou, Y.-P., Eds.; IntechOpen: Rijeka, 2017; Chapter 1.
- (49) Giannozzi, P.; Baroni, S.; Bonini, N.; Calandra, M.; Car, R.; Cavazzoni, C.; Ceresoli, D.; Chiarotti, G. L.; Cococcioni, M.; Dabo, I. et al. QUANTUM ESPRESSO: a modular and open-source software project for quantum simulations of materials. *Journal of Physics: Condensed Matter* **2009**, *21*, 395502.
- (50) Vanderbilt, D. Soft self-consistent pseudopotentials in a generalized eigenvalue formalism. *Phys. Rev. B* **1990**, *41*, 7892–7895.

- (51) Perdew, J. P.; Zunger, A. Self-interaction correction to density-functional approximations for many-electron systems. *Phys. Rev. B* **1981**, *23*, 5048–5079.
- (52) Thonhauser, T.; Zuluaga, S.; Arter, C. A.; Berland, K.; Schröder, E.; Hyldgaard, P. Spin Signature of Nonlocal Correlation Binding in Metal-Organic Frameworks. *Phys. Rev. Lett.* **2015**, *115*, 136402.
- (53) Thonhauser, T.; Cooper, V. R.; Li, S.; Puzder, A.; Hyldgaard, P.; Langreth, D. C. Van der Waals density functional: Self-consistent potential and the nature of the van der Waals bond. *Phys. Rev. B* **2007**, *76*, 125112.
- (54) Cooper, V. R. Van der Waals density functional: An appropriate exchange functional. *Phys. Rev. B* **2010**, *81*, 161104.
- (55) Berland, K.; Cooper, V. R.; Lee, K.; Schröder, E.; Thonhauser, T.; Hyldgaard, P.; Lundqvist, B. I. van der Waals forces in density functional theory: a review of the vdW-DF method. *Reports on Progress in Physics* **2015**, *78*, 066501.
- (56) Plimpton, S. Fast Parallel Algorithms for Short-Range Molecular Dynamics. *Journal of Computational Physics* **1995**, *117*, 1 – 19.
- (57) <https://lammps.sandia.gov>.
- (58) Adams, B.; Bauman, L.; Bohnhoff, W.; Dalbey, K.; Ebeida, M.; Eddy, J.; Eldred, M.; Hough, P.; Hu, K.; Jakeman, J. et al. DAKOTA, A Multilevel Parallel Object-Oriented Framework for Design Optimization, Parameter Estimation, Uncertainty Quantification, and Sensitivity Analysis: Version 5.4 User’s Manual. *Sandia Technical Report* **2009**, *SAND*, 2010–2183.
- (59) <https://dakota.sandia.gov>.
- (60) <http://www.physics.iisc.ernet.in/~mjain/pages/software.html>.

- (61) Wen, M.; Carr, S.; Fang, S.; Kaxiras, E.; Tadmor, E. B. Dihedral-angle-corrected registry-dependent interlayer potential for multilayer graphene structures. *Phys. Rev. B* **2018**, *98*, 235404.
- (62) Naik, M. H.; Jain, M. Origin of layer dependence in band structures of two-dimensional materials. *Phys. Rev. B* **2017**, *95*, 165125.
- (63) Zhao, Y.; Luo, X.; Li, H.; Zhang, J.; Araujo, P. T.; Gan, C. K.; Wu, J.; Zhang, H.; Quek, S. Y.; Dresselhaus, M. S. et al. Interlayer Breathing and Shear Modes in Few-Trilayer MoS₂ and WSe₂. *Nano Letters* **2013**, *13*, 1007–1015.
- (64) Chen, S.-Y.; Zheng, C.; Fuhrer, M. S.; Yan, J. Helicity-Resolved Raman Scattering of MoS₂, MoSe₂, WS₂, and WSe₂ Atomic Layers. *Nano Letters* **2015**, *15*, 2526–2532.
- (65) O'Brien, M.; McEvoy, N.; Hanlon, D.; Hallam, T.; Coleman, J. N.; Duesberg, G. S. Mapping of low-frequency raman modes in cvd-grown transition metal dichalcogenides: Layer number, stacking orientation and resonant effects. *Scientific reports* **2016**, *6*, 19476.
- (66) Maity, I.; Maiti, P. K.; Jain, M. Temperature-dependent layer breathing modes in two-dimensional materials. *Phys. Rev. B* **2018**, *97*, 161406.
- (67) Wang, H.; Liu, F.; Fu, W.; Fang, Z.; Zhou, W.; Liu, Z. Two-dimensional heterostructures: fabrication, characterization, and application. *Nanoscale* **2014**, *6*, 12250–12272.
- (68) Tongay, S.; Fan, W.; Kang, J.; Park, J.; Koldemir, U.; Suh, J.; Narang, D. S.; Liu, K.; Ji, J.; Li, J. et al. Tuning Interlayer Coupling in Large-Area Heterostructures with CVD-Grown MoS₂ and WS₂ Monolayers. *Nano Letters* **2014**, *14*, 3185–3190.
- (69) Liu, K.; Yan, Q.; Chen, M.; Fan, W.; Sun, Y.; Suh, J.; Fu, D.; Lee, S.; Zhou, J.; Tongay, S. et al. Elastic Properties of Chemical-Vapor-Deposited Monolayer MoS₂, WS₂, and Their Bilayer Heterostructures. *Nano Letters* **2014**, *14*, 5097–5103.

- (70) Gong, Y.; Lei, S.; Ye, G.; Li, B.; He, Y.; Keyshar, K.; Zhang, X.; Wang, Q.; Lou, J.; Liu, Z. et al. Two-Step Growth of Two-Dimensional WSe₂/MoSe₂ Heterostructures. *Nano Letters* **2015**, *15*, 6135–6141.
- (71) Liu, Y.; Weiss, N. O.; Duan, X.; Cheng, H.-C.; Huang, Y.; Duan, X. Van der Waals heterostructures and devices. *Nature Reviews Materials* **2016**, *1*, 16042.
- (72) Huang, S.; Liang, L.; Ling, X.; Puretzy, A. A.; Geohegan, D. B.; Sumpter, B. G.; Kong, J.; Meunier, V.; Dresselhaus, M. S. Low-Frequency Interlayer Raman Modes to Probe Interface of Twisted Bilayer MoS₂. *Nano Letters* **2016**, *16*, 1435–1444.
- (73) Puretzy, A. A.; Liang, L.; Li, X.; Xiao, K.; Sumpter, B. G.; Meunier, V.; Geohegan, D. B. Twisted MoSe₂ Bilayers with Variable Local Stacking and Interlayer Coupling Revealed by Low-Frequency Raman Spectroscopy. *ACS Nano* **2016**, *10*, 2736–2744.
- (74) Wu, F.; Lovorn, T.; Tutuc, E.; MacDonald, A. H. Hubbard Model Physics in Transition Metal Dichalcogenide Moiré Bands. *Phys. Rev. Lett.* **2018**, *121*, 026402.